Atomic-resolution chemical characterization of (2x)72-kDa tryptophan synthase via four- and five-dimensional ^{1}H-detected solid-state NMR

Alexander Klein[a,b], Petra Rovó[a], Varun V. Sakhrani[c], Yangyang Wang[c], Jacob B. Holmes[c], Viktoriia Liu[c], Patricia Skowronek[a], Laura Kukuk[b], Suresh K. Vasa[a,b], Peter Güntert[d,e,f], Leonard J. Mueller[c], and Rasmus Linser[a,b,1]

[a]Department of Chemistry and Pharmacy, Ludwig Maximilians University, 81377 Munich, Germany; [b]Department of Chemistry and Chemical Biology, TU Dortmund University, 44227 Dortmund, Germany; [c]Department of Chemistry, University of California, Riverside, CA 92521; [d]Institute of Biophysical Chemistry, Goethe University, 60438 Frankfurt am Main, Germany; [e]Laboratory of Physical Chemistry, Eidgenössische Technische Hochschule (ETH) Zürich, 8093 Zürich, Switzerland; and [f]Department of Chemistry, Tokyo Metropolitan University, Tokyo 192-0397, Japan

Edited by Robert Tycko, Laboratory of Chemical Physics, National Institute of Diabetes and Digestive and Kidney Diseases, Bethesda, MD; received August 12, 2021; accepted December 13, 2021

NMR chemical shifts provide detailed information on the chemical properties of molecules, thereby complementing structural data from techniques like X-ray crystallography and electron microscopy. Detailed analysis of protein NMR data, however, often hinges on comprehensive, site-specific assignment of backbone resonances, which becomes a bottleneck for molecular weights beyond 40 to 45 kDa. Here, we show that assignments for the (2x)72-kDa protein tryptophan synthase (665 amino acids per asymmetric unit) can be achieved via higher-dimensional, proton-detected, solid-state NMR using a single, 1-mg, uniformly labeled, microcrystalline sample. This framework grants access to atom-specific characterization of chemical properties and relaxation for the backbone and side chains, including those residues important for the catalytic turnover. Combined with first-principles calculations, the chemical shifts in the β-subunit active site suggest a connection between active-site chemistry, the electrostatic environment, and catalytically important dynamics of the portal to the β-subunit from solution.

solid-state NMR | NMR crystallography | tryptophan synthase | PLP-dependent enzymes | tautomerism

The family of pyridoxal-5′-phosphate (PLP)–dependent enzymes catalyze a wide variety of chemical transformations including transamination, racemization, decarboxylation, elimination, and substitution (1, 2). The large number of PLP enzymes and their crucial metabolic functions make them drug targets for the treatment of diseases including tuberculosis, epilepsy, and Parkinson's disease (3, 4). Fig. 1*A* depicts the crystal structure of *Salmonella typhimurium* tryptophan synthase (TS) (5). TS itself is both an important drug target in the context of continuously emerging bacterial antibiotics resistance (6) and of great interest in biotechnology (7) as an enantiospecific source of a large variety of unnatural amino acids and their derivatives (Fig. 1*B*) (8, 9). Wild-type TS catalyzes the final two steps in tryptophan biosynthesis: production of indole from indole-3-glycerol phosphate (IGP) and its subsequent condensation reaction with L-serine to give L-tryptophan (5, 10, 11). As for many other enzymes, X-ray structural data are abundant, but the rational design of therapeutic agents and the understanding and engineering of catalysis, in particular regarding the β-subunit enzymatic reaction, hinge on the availability of detailed knowledge of the chemical and electrostatic properties of the active site. Fig. 1*C* shows the initial steps of the β-subunit reaction, which acts as a pivot for the overall reaction and selectivity of the catalytic cycle. Nucleophilic attack of the PLP cofactor in the β-subunit active site is thought to involve activation of C4′ (Fig. 1*C*) by protonation of βLys87 Nζ. However, the thermodynamic and kinetic details of potential tautomeric exchange are currently missing (11–13). Such features, in particular protonation, hybridization, and tautomeric states of the active-site side chains and substrates, cannot be directly determined by protein crystallography or cryoelectron microscopy (cryo-EM) but are accessible from NMR chemical shifts.

NMR spectroscopy has been invaluable for addressing the chemical features and dynamics of molecules across disciplines. Mechanistic studies of enzymatic catalysis by NMR have been indispensable for complementing the insights from crystallography, cryo-EM, optical spectroscopy, and computational simulation (14–16). In addition to atomic-resolution access to protein dynamics and domain motion, the individual chemical shifts themselves are a prime source of information. Even though bulk properties from relaxation or diffusion measurements can sometimes be sufficient to address specific biological questions, the site-specific assignment of chemical shifts is a common prerequisite for elucidation of structure, dynamics, and interactions in more detail. For proteins exceeding a monomer molecular weight of 40 to 45 kDa, resonance assignments become a major bottleneck (17), as witnessed by the scarcity of proteins with substantial backbone assignments in this range

Significance

The atomic-level understanding of protein function and enzyme catalysis requires site-specific information on chemical properties such as protonation and hybridization states and chemical exchange equilibria. This information is encoded in NMR chemical shifts, which serve as important complementary information to structural data from other experimental techniques or structure prediction algorithms. This study demonstrates that comprehensive chemical-shift assignments are achievable for large and highly complex proteins, offering insights into chemical structure and dynamics. The access to the active-site chemistry in the 144-kDa (72-kDa asymmetric unit) enzyme tryptophan synthase demonstrated here extends the elucidation of chemical properties to a member of an important class of enzymes of interest in pharmacology and biotechnology.

Author contributions: L.J.M. and R.L. designed research; A.K., P.R., V.V.S., Y.W., J.B.H., V.L., P.S., S.K.V., P.G., and L.J.M. performed research; A.K., P.R., V.V.S., Y.W., J.B.H., V.L., P.S., L.K., S.K.V., L.J.M., and R.L. analyzed data; and A.K., L.J.M., and R.L. wrote the paper.

The authors declare no competing interest.

This article is a PNAS Direct Submission.

[1]To whom correspondence may be addressed. Email: rasmus.linser@tu-dortmund.de.

This article contains supporting information online at http://www.pnas.org/lookup/suppl/doi:10.1073/pnas.2114690119/-/DCSupplemental.

Published January 20, 2022.

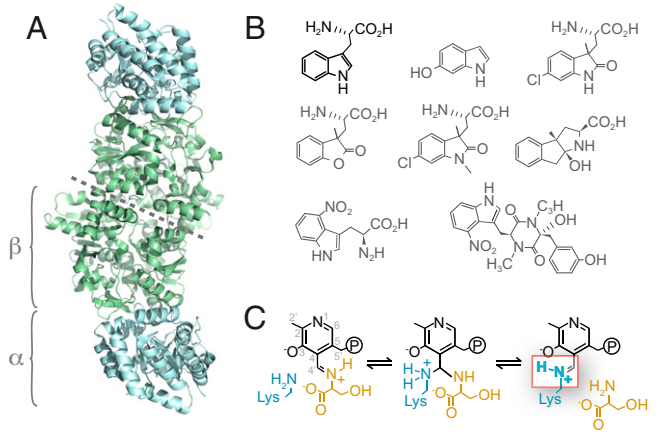

Fig. 1. TS is an αββα heterodimer with an asymmetric unit of 72 kDa. (*A*) Topology for the internal aldimine resting state (PDB ID: 4HT3) (5). (*B*) The natural product tryptophan (black) and a selection of additional substrates and products of engineered TS enzymes for biotechnological applications (gray). The lower right compound represents thaxtomin A, a natural product synthesized from 4-nitroTrp (*Lower Left*) (8, 9). (*C*) Initial step of the β-subunit catalytic cycle, drawn with a protonated βK87 Schiff base (red box).

(*SI Appendix*, Fig. S1). Site-specific amino acid labeling of canonical nuclei (18), the introduction of noncanonical probes such as ^{19}F (19), and the use of different types of methyl labeling (20) are examples of approaches used to strongly reduce the otherwise excessive spectral overlap in large proteins. Whereas such a reduction of complexity can be very potent to answer important biological questions even for extremely large systems, a wealth of common and versatile NMR approaches are tied to resonance assignment of the protein backbone, including backbone relaxation and relaxation dispersion, secondary structural propensities, H-N residual dipolar couplings, and H/D exchange. Other applications, such as high-resolution structure calculations, even rely on (close-to) complete resonance assignments of both backbone and side chains. In order to facilitate assignments, particularly as the size of the system increases, the resonances are usually dispersed by appending additional dimensions to multidimensional NMR experiments (21, 22).

Solid-state NMR (ssNMR) has been established as an atomic-level probe capable of providing insights into structure, intermolecular interactions, and dynamics in increasingly complex targets of higher effective (oligomeric) molecular weight (23–27). In particular, detailed insights have been obtained for supramolecular assemblies like virus capsids or large-scale cellular architectures (28), fibrillar proteins, including those associated with neurodegenerative diseases (29, 30), and membrane proteins within a lipid bilayer (31). Recently, innovations in sample preparation, most notably various deuteration strategies (32–35), paramagnetic doping (36–38), and hardware for increasingly fast magic-angle-spinning (MAS) (39–41), have led to a large pool of proton-detected ssNMR methodology. Combined with a series of smart spectroscopic approaches (42–46), this framework has been facilitating access to atom-specific chemical-shift assignments in increasingly challenging target proteins (25–27, 47, 48).

As the size of the target protein system increases, the number of molecules in the MAS rotor decreases. The corresponding decrease in signal intensity can, in principle, be compensated for by increased measurement times and the use of higher magnetic fields; even still, the increasing extent of resonance overlap and the resulting ambiguities in the assignment of proteins of high complexity remains a main limiting factor. Higher-dimensional ssNMR experiments have specifically been developed to ameliorate resonance overlap in spectral assignments (24, 45, 49–53), structure calculation (43, 54–56), and characterization of protein dynamics (53). Still, a wealth of proteins of medical, biological, or biotechnological interest remain significantly more complex than those accessible to NMR assignment to date, which calls for further methodological developments for characterization of high-molecular-weight targets.

As TS is an almost completely α-helical enzyme and has an asymmetric unit of 665 individual amino acids (72 kDa) and a molecular weight of 144 kDa for the full αββα complex, chemical-shift assignments have been available only for specifically labeled cofactor, substrates, and individually labeled residues (5, 11, 13, 57–59). To enable chemical-shift assignments for access to site-specific chemical properties and other downstream NMR analyses of TS, we introduce a higher-dimensionality ssNMR approach based on proton-detected, fast-MAS ssNMR spectroscopy. Focusing specifically on the β-subunit active site, this strategy reveals important features of residue βK87, which holds the PLP cofactor. In particular, the active site's chemical nature is characterized by the Schiff base comprising a fast tautomeric exchange between the protonated and unprotonated forms (red box in Fig. 1*C*). This tautomeric equilibrium, moreover, appears to be coupled to variations of the pocket architecture on an intermediate timescale consistent with substrate transport and trapping.

Results

Access to Complex Target Proteins via ^{1}H-Detected, Fast-MAS ssNMR. Higher-dimensionality (>3D [three-dimensional]) experiments are a direct approach to increasing the effective resolution of NMR correlation experiments. For example, Fig. 2*B* demonstrates the increase in dispersion for backbone experiments from 3D to 5D for TS, which comprises strong overlap in the 2D H/N plane (Fig. 3*A*). However, sensitivity typically suffers from the multitude of transfer steps and evolution periods required when going to higher dimensionality. Compared to the exponentially decreasing transfer efficiency with molecular size in solution, however, ssNMR polarization transfer efficiency is independent of molecular weight (45, 60). This, in conjunction with the associated long coherence lifetimes and the absence of high-power decoupling, makes proton-detected, fast-MAS ssNMR approaches well suited when complex (and, in particular, higher-dimensionality) experiments are desired (Fig. 2*C*). For NMR experiments exceeding three dimensions, nonuniform sampling (NUS; used here with down to <0.01% sampling density) and spectral reconstruction are commonly used to accelerate data acquisition (24, 48, 50, 52, 54, 55), allowing the experimental time to be determined by sensitivity instead of resolution. The approach of automated projection spectroscopy, which is compatible with the same pulse sequences as shown here, shares a similar goal and has been shown to facilitate assignment in cases in which peak picking in 2D source spectra is possible (45, 61).

Experimental Strategies. For assignment and downstream analysis in TS, we used a triple-labeled, proton back-exchanged, and Cu-edta–doped microcrystalline sample (*Materials and Methods*). For residue linking, we first employed 4D experiments for carbon match making [hCACONH and hCOCANH (24, 50, 51), green/cyan in Fig. 2*A*, and hCACBcaNH and hCACBcacoNH, yellow/red, constructed from existing 3D schemes (62–64) via additional chemical-shift evolution on Cα and full magnetization transfer between Cα and Cβ]. Such carbon-based approaches (64, 65) usually involve 1) finding a given CC combination from a first experiment within a second one and 2)

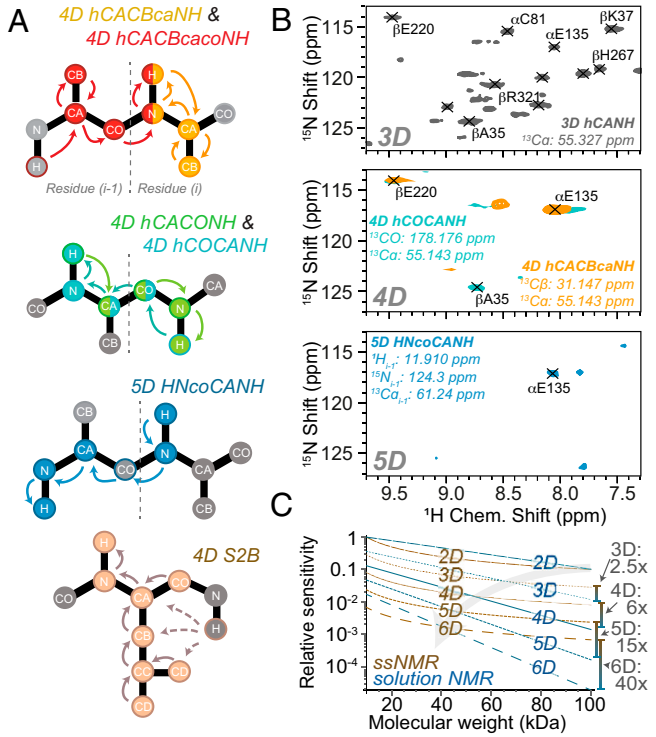

Fig. 2. Strategies employed for site-specific resonance assignment of TS. (*A*) Magnetization pathways for the 4D hCACBcaNH/hCACBcacoNH and 4D hCACONH/hCOCANH pairs, the 5D HNcoCANH, and the 4D S2B [side chain-to-backbone] experiment (with a 4D hCCNH pathway). All experiments are cross polarization (CP) based; only for Cα/Cβ transfers INEPTs (Insensitive Nuclei Enhanced by Polarization Transfers) were employed. For the S2B experiment, MOCCA was used for mixing, and both proton and carbon polarization was enCOPORADEd (COmbined POlarization from long-Range transfer And Direct Excitation) (72, 73). (See all acquisition and processing parameters in *SI Appendix*.) (*B*) The gain in dispersion for higher dimensionality witnessed for αE135 as a representative residue in the overlapping region between 8 and 10 ppm, comparing three (*Top*, 3D hCANH in gray), four (*Center*, 4D hCOCANH in cyan and 4D hCACBcaNH in yellow), and five dimensions (*Bottom*, 5D HNcoCANH in blue) (noncrossed peaks: maxima in clearly different planes). All experiments were recorded on a deuterated and ^{1}H-back-exchanged, ^{13}C/^{15}N-labeled sample at 700 MHz proton Larmor frequency at 55 kHz MAS and 30 °C in a 1.3-mm rotor. (*C*) Generic assessment of the growing benefits of ssNMR for increasingly complex experiments (in particular, increasing dimensionality) as a function of molecular weight, relative to simple 2D correlations for a 10-kDa protein in the respective aggregation state. (Details of the parameters used are in *SI Appendix*, Section 2.) Gray arrow: trend for molecular weights of break even; numbers on the right: trends for sensitivity advantages over NMR in solution at 100 kDa (monomeric protein), increasing with experiment complexity.

finding the H/N coordinates associated there again in the first experiment. Hence, the ambiguity for identifying the next H/N corresponds to the overlap within a 3D Cα/Cβ/CO, and the correct selection of the next CCC combination is ruled by 2D H/N dispersion.

We (and, simultaneously, the Pintacuda laboratory) previously developed sensitive amide-to-amide correlation experiments (HNCOCANH-type experiments) in three and four dimensions (53, 66, 67), which have also been exploited for projection spectroscopy in the solid state (45). The direct linking between amides in such experiments circumvents any ambiguity of CC matching steps, which is an important aspect in TS, given that here, even Cα/CO/Cβ triple overlap occurs for 65% of the residues (Fig. 3*D* and *SI Appendix*, Fig. S3) and that each ambiguity scales the number of possibilities in an exponential fashion. In the case of overlapping H/N signals, however, ambiguity remains that can only be resolved in a combinatorial way in conjunction with the residue type information associated with ^{13}C shifts. These are, however, absent in 4D HNcocaNH-type experiments, such that the connection of sequential linking and residue type is again diffused by the level of H/N overlap. Therefore, we expanded HNCOCANH-type experiments to NUS 5D experiments. Like their 3D/4D counterparts, the 5D HNcoCANH (Fig. 2*A*, blue)—or, likewise, the (inverted) HNcaCONH—each allow for a backbone walk based on amide-to-amide connectivities individually (Fig. 3*B*), however, now identifying a source residue by H/N/C shifts (i.e., three rather than two dimensions) and identifying its neighbor by H/N shifts (two further dimensions). This renders one out of the two connected residues (the source residue) rather unambiguously characterized, as the H/N/Cα triple facilitates correlating it with the set of side chain shifts and thus residue type. (The overall extent of H/N/CA overlap in TS is 3× lower than H/N overlap; see Fig. 3*E*.) This combination between sharp sequential connectivities and the residue type–specific knowledge for ^{13}C shifts with intrinsically correct referencing enables short strips of sequential connections obtained from these five-dimensional experiments to be mapped onto the known primary sequence and makes this experiment more potent than the respective 4D version. HNcoCANH and HNcaCONH pathways can be set up with a high bulk sensitivity of ∼8% and ∼5%, respectively, relative to an hNH (compare *SI Appendix*, Figs. S6 and S9*B*). The 5D NUS data were treated as established for solution NMR (brief description in *SI Appendix*, Section 6) using sparse multidimensional Fourier transformation (SMFT) (68) (Fig. 3*C*). *SI Appendix*, Section 7 shows the setup of both sequences for the case of the SH3 domain of chicken α-spectrin, including a high-quality 5D dataset obtainable (for this 7.2-kDa protein) in only 1.5 d (*SI Appendix*, Fig. S7).

Whereas backbone assignments have been playing a major role for proton-detected ssNMR, side chain nuclei exceeding the usual Cβ have mostly been ignored in recent methodological efforts. This is despite their obvious significance for structure calculation (41, 69–71), as a reporter on protein chemical features and interactions, and their value for residue type information. Here, we generated a 4D hCCNH version of the side chain-to-backbone (S2B) experiment (42, 53, 72) based on modified phase-cycled Carr–Purcell (MOCCA) mixing (72, 73) (beige in Fig. 2*A*), which we had proposed in a 3D fashion originally. The 4D hCCNH experiment yields the set of side chain carbons (in one dimension) dispersed by their H/N/Cα shifts in one additional dimension each. Finally, 2D H/C correlations and variable-temperature H/N spectra were acquired. Further material on assignment strategies, all pulse schemes and acquisition parameters, and a comparison of bulk signal intensities for the individual experiments are shown in *SI Appendix*, Sections 3–5, respectively. *SI Appendix*, Section 7 gives examples for the inverted HNcaCONH pulse sequence. In addition, we used pseudo-4D, $R_{1\rho}$-edited hCONH experiments to warrant reasonable dispersion in a first assessment of TS relaxation. (See considerations on dimensionality in assignment versus relaxation experiments in *SI Appendix*, Section 8.) As the assignment process of TS was still a large effort, even with the multitude of data sets available, systematic evaluation of the quantitative benefits of each individual dataset could only be performed with respect to the combinatorial/statistical assessments presented.

Assignment of TS. Assignments were supported by state-of-the-art computational capability via FLYA (74). Modifications (magnetization pathways, tolerances for chemical-shift matching, validation criteria, etc.) are described in detail in *SI Appendix*, Section 10. This computationally aided strategy enables a residue-specific, quantitative assessment of assignment quality in

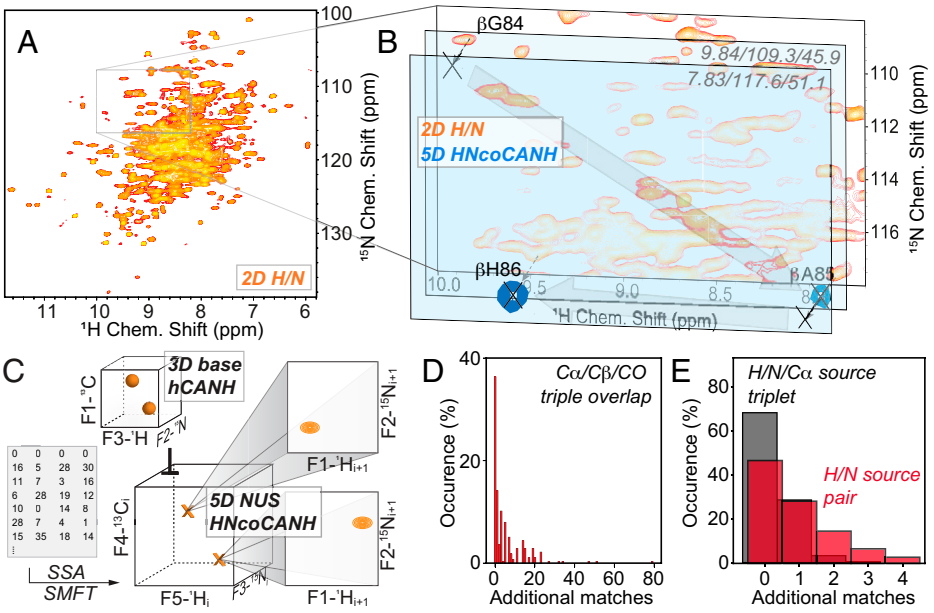

Fig. 3. Higher-dimensionality ssNMR for assignment of TS. (*A*) The 2D H/N correlation of TS (proton–back-exchanged, perdeuterated at 55 kHz MAS and 700 MHz ^{1}H Larmor frequency). (*B*) Backbone walk via a 5D HNcoCANH (blue), shown via gray arrows for βG84 to βH86 in their respective 2D H_{i+1}/N_{i+1} slices (taken from $H_i/N_i/C\alpha_i$ coordinates as depicted in the upper right corner), overlayed on the H/N plane. The full set of experiments recorded is shown for these residues in *SI Appendix*, Fig. S3. (*C*) Acquisition and processing of the 5D HNcoCANH, acquired as a sparse NUS dataset and reconstructed via SSA (89) in conjunction with a 3D hCANH experiment that shares the $C\alpha_i$, $^{15}N_i$, and $^{1}H_i$ dimensions with the 5D. Fourier transformation is performed by SMFT (68), generating two-dimensional $^{1}H_{i+1}$ (F1)/$^{15}N_{i+1}$ (F2) planes at F3/F4/F5 *i* positions derived from the 3D peak list (also *SI Appendix*, Section 6). (*D*) Occurrence of assignment ambiguity within all of three carbon chemical shifts (as used in common, ^{13}C-match-making assignment experiments) for TS, only considering assigned shifts. (*E*) Ambiguity upon linking experiments that provide residue type information (e.g., hCACBcaNH or hCCNH) with either H/N only (dark red) or H/N/Cα (gray) shifts, which are the shift combinations available from sequential linking via either 4D or 5D amide-to-amide correlations, respectively. See details in the *SI Appendix*, Fig. S2 caption. In *D* and *E*, the *y*-axes are normalized to the overall number of residues assigned sufficiently.

an iterative way. Reliable assignment benefits from the high redundancy introduced by the combination of multiple, mutually consistent higher-dimensionality approaches. (*SI Appendix*, Fig. S3 shows a set of spectral excerpts for an exemplary stretch of residues.) In total, chemical-shift assignments were obtained that enable potential downstream analyses for up to 498 residues (74.8% of the 665 total residues or 79.0% of the 630 nonproline residues). Fig. 4 depicts the backbone chemical-shift assignments of TS that satisfy highly conservative validation with stringent exclusion criteria in FLYA with respect to next-neighbor assignments (details in *SI Appendix*, Section 10). Missing residues, other than prolines, derive from assignment ambiguity or insufficient intensity upon reconstruction due to exchange broadening or H/D back-exchange. Chemical-shift tables can be found in *SI Appendix*, Section 15 as well as under Biological Magnetic Resonance Data Bank (BMRB) entry 51166 (75) .

NMR chemical shifts are direct reporters on the chemical and electrostatic properties of individual sites within the protein. The chemical-shift values of side chain moieties in particular are shaped by their individual protonation, tautomerization, and H-bonding properties. Conversely, such features can be inferred when shifts have been determined. Chemical-shift data represent the foundation for investigating the catalytic mechanism, often with assistance from crystallography and first-principles calculations (5, 11, 57, 58, 59). Here, we exploit the availability of TS chemical-shift assignments to advance insights into the β-subunit active site, in particular residue βK87, at physiological temperatures. βK87 is a key residue of the β-subunit catalytic pocket, initially holding the PLP cofactor and later serving as the acid–base catalyst (10). Full βK87 chemical-shift assignments began with the proton-detected 4D and 5D sequential backbone experiments, and these in turn enabled side chain carbon assignments (from Cα through Cε) via the 4D hCCNH, which link to Nζ (the Schiff base nitrogen) and the Hζ proton in the H/N via a long-range H/C correlation (Fig. 5 and Table 1). The entirety of the βK87 shifts give direct experimental access to the question of the linking Schiff-base equilibrium protonation state and the associated energies (10).

The Protonation State of βK87 Nζ. Protonation of the Schiff-base nitrogen, Nζ, has been proposed to activate the cofactor C4′ carbon for nucleophilic attack by the incoming substrate, serine (Fig. 1*C*) (11–13). How this activation might be coupled to larger conformational motions responsible for substrate trapping and allosteric signaling remains an intriguing mechanistic question. Here, the intermediate value of 227.3 ppm found for Nζ at 30 °C suggests a dynamic tautomeric exchange between protonated and neutral Schiff-base forms (11). To quantify the exchange and the identity of the chemical structure of the exchanging partners, we turned to NMR-assisted crystallography—the integrated application of ssNMR, X-ray crystallography, and first-principles computational chemistry (11, 26, 44, 57, 59, 76–81).

Our approach follows that of Caulkins et al. (11). Starting with the crystal structure of the TS internal-aldimine form (Protein Data Bank identifier [PDB ID]: 4HT3), a cluster model of the active site was constructed that included all residues within 7 Å of the PLP cofactor. Five models of the active-site chemistry were generated by varying the protonation states of the pyridine ring nitrogen, pyridoxal phenolic oxygen, and Nζ of βLys87 (*SI Appendix*, Scheme S1). Each of these candidate structures was geometry optimized using density functional theory (DFT), with the exterior residues of the cluster fixed at their crystallographic positions. NMR chemical shieldings were calculated using a locally dense basis approach and converted to chemical shifts (82) (*SI Appendix*, Table S6). Finally, the structural models were ranked based on the agreement

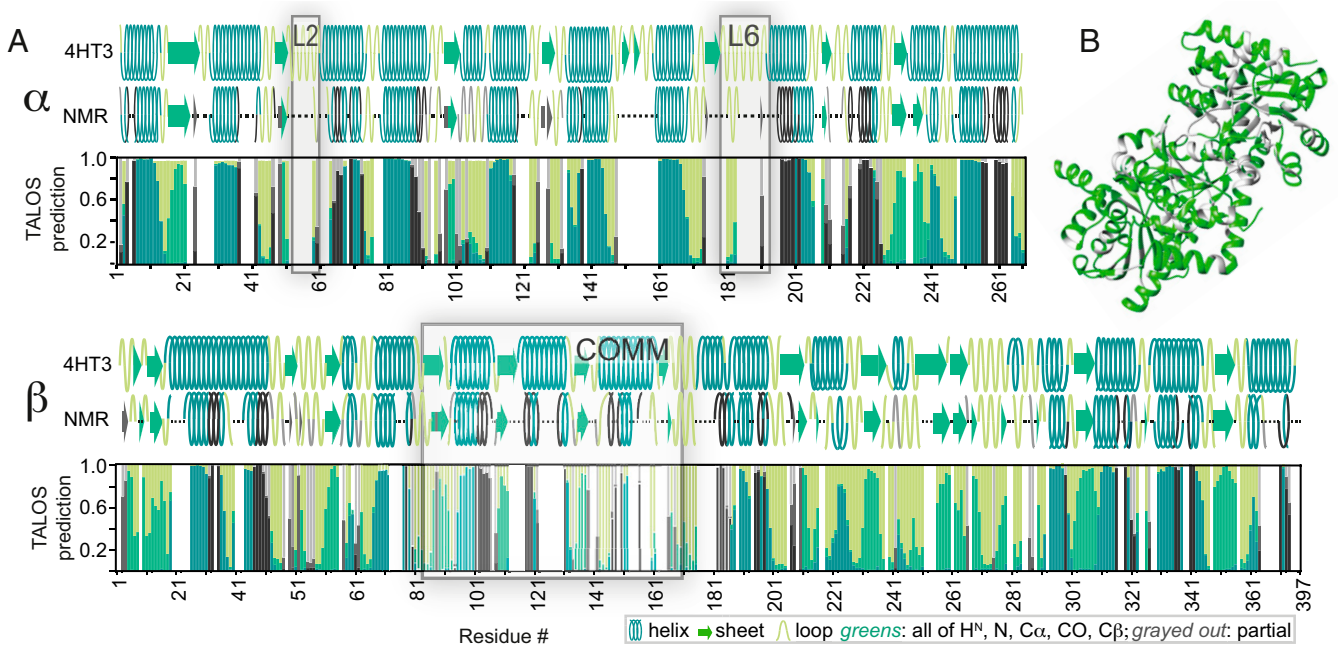

Fig. 4. Chemical-shift assignment in TS from ssNMR. (*A*) Assigned residues for the α- (*Top*) and β-subunit (*Bottom*) and analysis with respect to the secondary structure predicted by TALOS-N (90). Cyan to green colors denote high-confidence assignment in modified FLYA quality assessment, requiring all of H^N, N, Cα, CO, and Cβ of a residue to be individually assigned as "strong," which rating itself is defined very conservatively as detailed in *SI Appendix*, Section 10. Gray tones denote that a subset of the five nuclei within a residue are designated as "strong" assignments, whereas the remaining nuclei of the residue have shifts that are likely correct also but do not reach the same confidence level. TALOS predictions are compared with secondary structure found in crystals structure 4HT3 (5) (*Top*). Boxes highlight domains considered to undergo major conformational changes upon ligand binding at different states of the catalytic cycle (5), also bearing low assignment coverage. Mismatches between TALOS predictions and the crystal structure are expected for residues with incompletely assigned shifts, at the edges of assigned regions, and for short stretches (e.g., β233 to β243 or β261 to β265), while secondary chemical shifts (*SI Appendix*, Fig. S10) are usually consistent. (*B*) Residues with strong assignments for all of the above-mentioned nuclei marked on the asymmetric unit (630 nonproline residues) of the crystal structure (green, PDB ID: 4HT3).

between their first-principles predicted chemical shifts and the ssNMR assignments for the βLys87 side chain and PLP cofactor using the reduced-χ^2 statistic, the weighted deviation of the model from experimental shifts.

Of the candidate structures, none was found to show acceptable agreement between the predicted and experimental chemical shifts, with the lowest reduced $\chi^2 = 28.4$ (*SI Appendix*, Table S6). Based on the temperature dependence and large line width of the

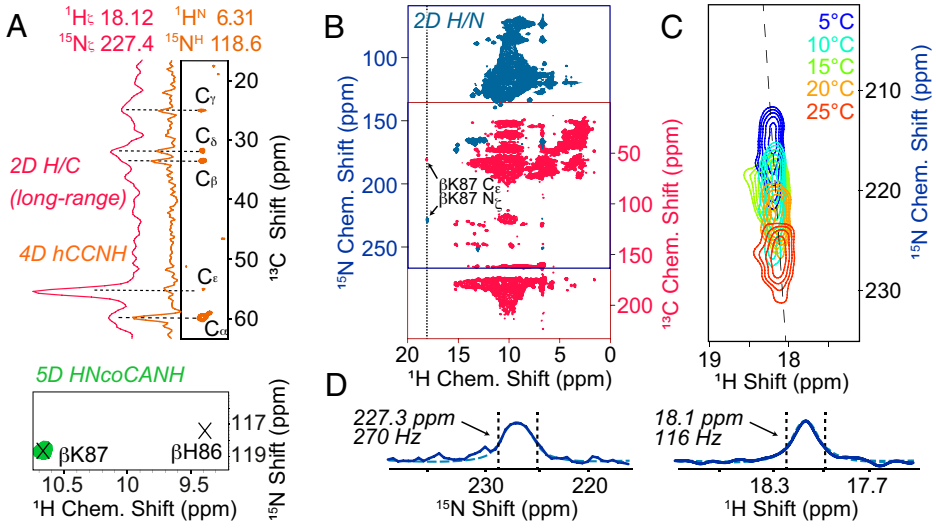

Fig. 5. NMR assessment of the catalytically important residue βK87. (*A*) Backbone and side chain carbon assignment, respectively, via 5D HNcoCANH (green) and 4D hCCNH (yellow). (*B*) The 2D H/N correlation (blue) and 2D long-range H/C correlation (magenta). The cross-section along the ^{13}C axis (dotted line) is plotted in magenta in *A*. (*C*) Temperature-dependent H/N correlations of the Schiff base, achieved by measurements of the same (deuterated) protein sample in a 0.7-mm rotor at 55 kHz MAS. (*D*) Cross-sections for the ^{15}N of the Schiff base (Nζ, *Left*) and its proton (*Right*), spectrum with 50 Hz exponential decay and Lorentzian as solid and dashed lines, respectively for line shape analysis/determination of exchange rates. The plane from the 5D HNcoCANH depicted in *A* is extracted at βH86 H,N,Cα shifts 9.44/117.1/58.9, with the ^1H coordinates shown folded in from 6.3 ppm (indirect H^N).

Table 1. Experimental and first-principles predicted chemical shifts (in ppm) for the PSB, phenolic, and their best-fit two-site exchange (61% PSB, 39% Phen) models at 30 °C

	Atom	PSB	Phen	Two-site exchange	Experimental
PLP	N1	304.4	302.7	303.7	294.7
	C3	173.9	158.8	166.0	168.3
	C2	162.0	153.3	158.6	159.6
	C2′	23.3	22.2	22.9	20.4
βLys87	Nζ/SBN	166.8	319.3	226.6	227.3
	Cγ	25.8	26.3	26.0	25.9
	Cδ	34.0	35.6	34.7	32.7
	Cε	50.7	57.6	53.4	53.3
	Red-χ^2	28.4	66.6	1.3	—*

*Red-χ2 is the reduced χ2 value between the set of experimental chemical shifts (rightmost column) and the set of shifts calculated for each model.

Schiff-base nitrogen (Fig. 5 *C* and *D* and *A Modulated Tautomeric Exchange*), fast-exchange equilibrium models were considered next, in which the effective chemical shifts were given as the population-weighted average of the shifts for the individual structures. All models were paired and their populations optimized for best agreement with the experimental chemical shifts. The best-fit fast exchange, with a reduced χ^2 of 1.3, was found to be between the protonated Schiff base (PSB; ketoenamine) and phenolic (Phen; enolimine) forms (Fig. 6*A*). Table 1 summarizes select experimental and first-principles predicted shifts for this model compared with its parent states. The next-best exchange model had a reduced χ^2 of 4.9, making it statistically unlikely (*SI Appendix*, Table S7). Bayesian probability analysis (83) confirmed that the best-fit exchange model is the most probable experimental state with 91% confidence (Fig. 6*B* and *SI Appendix*, Section 11).

NMR-assisted crystallography of the TS internal-aldimine state reveals a fast-exchange equilibrium between the PSB and phenolic forms. At 30 °C, the equilibrium populations are 61% and 39%, respectively, indicating an effective free-energy difference of only 1.2 kJ/mol between the tautomers and demonstrating the PSB to be the dominant, but not exclusive, form at physiologically relevant temperatures.

A Modulated Tautomeric Exchange. The populations of PSB and phenolic tautomers are strongly temperature dependent (Fig. 5*C*), which is unexpected for a simple two-state model for the exchanging proton and requires a significant entropy term to accommodate. (See the fit of enthalpy/entropy contributions to the free-energy difference in Fig. 6*C* and *SI Appendix*, Section 12.) The temperature dependence of the populations is, however, consistent with larger-scale processes in the surrounding active site being coupled to this exchange. Crystal structures of TS show both open and closed conformations of the β-subunit for various intermediates in the catalytic cycle (*SI Appendix*, Fig. S13) (2). The open conformation is necessary for the free diffusion of substrate into the active site. It also establishes an aqueous environment proximal to the cofactor that favors the Zwitterionic, PSB form (11). Closed conformations largely exclude water from the active site, favoring the neutral Schiff base, phenolic form. The open and closed states of the active site remain in equilibrium, with a switch between the predominant form for the various intermediates (5). An entire conformational exchange through the crystallographic conformations is unlikely in the absence of a substrate. However, it is noteworthy that already within a single (cryogenic) X-ray structure (PDB ID: 4HT3), conformational plasticity is seen in the entry portal for serine in the β-subunit active site (*SI Appendix*, Fig. S14), which involves interactions between residues in the carboxy-terminal α-helix and the loop holding the cofactor (*SI Appendix*, Figs. S14 and S15). Likewise, an isolated tautomeric-exchange process would be associated with a low effective activation barrier and an expected timescale in the picosecond-to-nanosecond regime (84, 85). To assess the effective timescale of the tautomeric exchange in the enzyme and whether contributions from conformational motion in the surrounding could play a role, we conducted line shape analysis of the Schiff-base nitrogen based on the limiting chemical shifts given by the computational modeling as well as $R_{1\rho}$ analysis of the protein backbone via the pseudo-4D, relaxation-edited hCONH experiments (details in *SI Appendix*, Sections 8 and 12). Line shape analysis gives experimental access to the apparent rates of the tautomeric exchange and hence, via the Eyring equation, the effective free energy of activation. Whereas homogeneous nitrogen line widths in the sample in the absence of exchange (including the βK87 backbone amide) generally amount to only around 20 Hz, linewidths for the Schiff-base nitrogen are on the order of 270 Hz (Fig. 5*D* and *SI Appendix*, Fig. S13). Equally, the Schiff-base proton has a line width of 120 Hz compared to amide H^N widths of, generally, around 50 Hz. Assuming a two-state exchange, the exchange-broadened lines suggest a tautomeric turnover on the microsecond motional timescale, with a forward rate of around 2.4×10^6 s^{-1}, a regime much slower (or a $\Delta G^{\ddagger}$ larger) than expected for an isolated proton-exchange process (84, 85). Even though the ssNMR line width does not purely reflect the

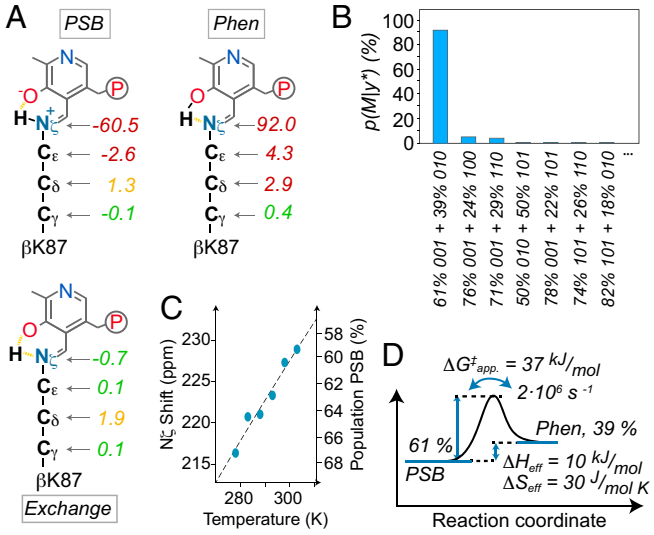

Fig. 6. Analysis of the tautomeric equilibrium at the βK87 Schiff base in the active site of the β-subunit. (*A*) Shifts obtained from first-principles calculations for the active site with PSB, protonated phenolic oxygen (Phen), and tautomeric exchange between the two with a 61:39 ratio. Numbers denote differences with respect to experimental chemical shifts in parts per million (ppm). (*B*) Bayesian probability for the best-fitting combinations of different two-site, fast-exchange equilibrium models, comparing experimental and first-principles chemical shifts, with protonation being denoted by "*1*" or "*0*", respectively, in order (*pyridine nitrogen*), (*phenolic oxygen*), (*Schiff base nitrogen*). (*C*) Best fit of temperature-dependent populations to the apparent enthalpy and entropy difference for the entire tautomeric exchange process within the enzyme. The dashed curve shows the dependence consistent with $\Delta H_{app.} = 9.6 \pm 1$ kJ/mol and $\Delta S_{app.} = 28.6 \pm 3$ J/(mol K). (Populations are derived from temperature-dependent $^{15}N\zeta$ chemical shifts measured in a 2D fashion but with universal carbon shifts.) (*D*) Effective energy profile of the tautomeric exchange of the Schiff base at 30 °C, reflecting both the equilibrium with the PSB slightly dominating, as well as the exchange rate and apparent activation energy of the process. Both the temperature dependence of populations and tautomeric exchange rate hint to association of the protonation/deprotonation of the Schiff base with changes in its environment in the pocket.

exchange contribution as in solution NMR and would have to be scaled down somewhat (to account for residual anisotropic interactions, sample inhomogeneity, and anisotropic bulk magnetic susceptibility) (86), the high apparent effective activation barrier is in line with the Nζ temperature dependence and consistent with a linkage of tautomerism with variations in the surrounding electrostatic environment. Details of conformational exchange dynamics can be provided by relaxation dispersion experiments, which have remained exceedingly demanding for TS so far. However, the simple $R_{1\rho}$ experiments at least reveal moderately elevated rates (5 to 9 s^{-1}, compared to rates of 1 to 2 s^{-1} for inconspicuous residues) at ∼30 °C for entry portal residues like D649 and G352 (rates in *SI Appendix*, Fig. S15, and relaxation decays in *SI Appendix*, Section 15). The increased rates, and likely also the low degree of assignments in the adjacent communication domain residues, are in agreement with the exchange-broadened character of the Schiff-base line shapes. Whereas details of the modulation of the exchange by the environment remain elusive, the data are consistent with a connection between tautomerism and a variable pocket environment, which suggests a modulation of Schiff-base protonation by the surrounding architecture. Possible scenarios in the functional enzyme would be a conformation-dependent fast-exchange equilibrium of the Schiff base directly driven by electrostatics or changes in the water network that differentially stabilize neutral and Zwitterionic forms dependent on pocket conformations and thus indirectly tune the Schiff base properties. These provide one possible mechanism for coupling global structural changes with chemical reactivity as part of the allosteric regulation in TS.

Discussion

The chemical shift in NMR is a sensitive probe of the individual chemical environment of a given atom, reporting on protonation state, hybridization state, hydrogen bonding interactions, and the surrounding electrostatic environment. With structure determination more and more facilitated by automation and computation, the addition of chemical shifts will become increasingly interesting for targets in various scientific disciplines. Chemical-shift measurements in enzymes have been the preeminent tool for characterizing the chemical structures of intermediates throughout the catalytic cycle, highlighting the protonation states and associated tautomeric equilibria for the cofactor, substrates, and active-site residues (10, 11, 13, 57, 59, 87). For enzymes as complex as TS, this approach has been limited to distinct, selective incorporation of ^{13}C and ^{15}N spin labels. Whereas individual shifts from specific labeling have often been sufficient for important insights, access to all shifts in (almost) the entire protein from a single preparation can yield a large number of individual insights (regarding interactions, residue-specific structural, motional, and chemical properties) at once, which can be beneficial from a biological as well as from a preparative perspective.

As the use of chemical shifts as restraints in first-principles computational refinement hinges on priors from real, experimentally obtained shifts, a high level of comprehensiveness for the chemical-shift data obtained through extensive assignments on U-^{13}C,^{15}N-labeled samples ushers in far-reaching possibilities for NMR-assisted crystallography that we expect will allow it to expand beyond the active site to include extended hydrogen bonding and proton transfer pathways, conformational dynamics, and allostery. In addition to simultaneous characterization of multiple shifts combined with complementary data on dynamics as becoming possible here, comprehensive assignments will also allow access to interactions with/distances to small molecules, substrates, and water, to other relaxation parameters, and to conformational assessment of individual residues or atoms. We anticipate that the analysis pursued for the TS resting internal-aldimine state studied here can be readily extended to other stable intermediates along the catalytic pathway, facilitated by the fact that the additional intermediates would not largely alter the chemical shifts for the majority of the enzyme and the bulk of the information can be utilized.

The assignments in TS are paradigmatic and foreshadow the value of ssNMR data for other high-molecular-weight targets in biology, pharmacological research, and biotechnology for which (micro)crystalline samples can be obtained. For example, common drug targets, including many kinases, phosphatases, nuclear receptors, and many membrane proteins like surface receptors, channels, and transporters, are often in a molecular-weight range of 60 to 80 kDa. Similarly, the monomeric molecular mass of many biocatalysts in industrial applications like dehydrogenases, lipases, and esterases often fall into this molecular-weight regime. With a moderate magnetic field of 16.5 T (700 MHz) used in this study, the assessment of TS has been a challenge, but decreasing measurement times by several fold would each apply for higher magnetic fields or with emerging MAS cryoprobes (88), which, coupled together, could shorten measurement times by up to an order of magnitude. As a drawback in comparison to carbon detection methods, prolines (and also side chain nuclei of aromatic residues) escape all of the assessments. In addition, incomplete back-exchange into the deuterated sample is a common drawback for proton- (H^N-)detected ssNMR both here as well as for other large proteins in which unfolding/refolding protocols fail. *SI Appendix*, Section 13 shows first spectra and sensitivities obtained for a nondeuterated TS sample spun at 111 kHz MAS in a 0.7-mm rotor, a framework that can circumvent both of these problems. In fact, very similar experiments are possible as for deuterated samples, as exemplified by a 4D hCOCANH experiment recorded for comparison (*SI Appendix*, Fig. S16). Lower sensitivity due to reduced sample volume (∼0.5 μL) and transfer efficiencies is noted but will benefit from the same advances in field strength and cryoprobes mentioned above.

Conclusion

Here, we have shown a protein ssNMR study enabled by higher-dimensionality (4D and 5D) shift assignments in the 144-kDa TS bienzyme complex with an asymmetric unit of 72 kDa. The benefits of higher dimensionality required for the 665-residue asymmetric unit, in particular low-ambiguity sequential correlations directly concatenated with side chain shifts and residue type data, are enabled by proton-detected fast-MAS ssNMR. The success of this approach is owed to high transfer efficiencies that are independent of molecular weight; thus the concatenation of many transfer steps and evolution periods within complex experiments at low duty cycles becomes possible. In combination with state-of-the-art computational approaches, the chemical shifts provide access to chemical, thermodynamic, and kinetic parameters for active-site species and give experimental insight into the interplay between plasticity, essential for substrate trapping and product release, and chemical properties within the pocket. The data reveal the dominance of a protonated Schiff-base species under physiological temperatures, with a tautomeric dynamic equilibrium that is linked to the electrostatic environment of the pocket architecture. This study demonstrates the feasibility of NMR assignment and assessment of dynamics and chemical properties in highly complex targets with minimal amounts of uniformly labeled protein. Facilitated access to NMR data in this molecular-weight regime will unlock an atomic-level understanding of reaction thermodynamics and kinetics widely sought for biological, medical, and industrial applications.

Materials and Methods

Salmonella typhimurium TS was expressed and purified as described in detail in *SI Appendix*, Section 14. In brief, *Escherichia coli* CB149 in M9 minimal medium was used with a pEBA-10 plasmid, and the protein was purified via a

crystallization and recrystallization procedure in the presence of Cs^+, polyethylen glycol-8000, and spermine in Tris buffer at pH 7.8. The SH3 domain of chicken α-spectrin was expressed and purified as described before (36). NMR spectra for SH3 and TS were acquired each on a single microcrystalline sample of a Cu-edta–doped, uniformly $^2H/^{13}C/^{15}N$ triple-labeled and 100% exchangeable-proton back-exchanged preparation. NMR spectra were recorded using a 1.3-mm probe at an MAS frequency of 55 kHz MAS at ∼30 °C effective temperature, using recycle delays of 0.6 s on a Bruker NEO spectrometer with a proton Larmor frequency of 700 MHz. All assignment experiments were performed as NUS experiments. All new pulse sequences for the 4D and 5D backbone and side chain assignment experiments, a list of acquisition and processing parameters, and practical considerations for setting up and processing NUS 5D ssNMR are found in *SI Appendix*, Sections 3–7.

First-principles geometry optimization and chemical-shift calculations for the TS resting state (internal aldimine) β-subunit active site were conducted using a DFT cluster-based approach following that of Caulkins et al. (11) as detailed in *SI Appendix*, Section 11. All chemical-shift assignments can be found under BMRB entry 51166.

Data Availability. Chemical-shift data have been deposited in the BMRB under entry 51166 (75). All other study data are included in the article and/or *SI Appendix*.

ACKNOWLEDGMENTS. We thank the group of W. Koźmiński and Jan Stanek for helpful discussions about Signal Separation Algorithm (SSA) and related processing scripts. R.L. was funded by the Deutsche Forschungsgemeinschaft (DFG, German Research Foundation) – 27112786, 325871075, and the Emmy Noether program. This study was funded by the DFG under Germany's Excellence Strategy – EXC 2033 – 390677874 – RESOLV and EXC-114 – 24286268 – CiPS-M (Ruhr Explores SOLVation and Center for integrated Protein Science Munich, respectively). Financial support is also acknowledged from US NSF Grant CHE1710671 and NIH Grants GM097569 and GM137008 given to L.J.M. We acknowledge the computing time provided on the Linux High-Performance Computing cluster at Technical University Dortmund (LiDO3), partially funded via the Large-Scale Equipment Initiative by the DFG as Project 271512359. Additional computations were performed using the computer clusters and data storage resources of the University of California, Riverside High-Performance Computer Cluster, funded by grants from NSF (MRI-1429826) and NIH (S10OD016290).

1. A. C. Eliot, J. F. Kirsch, Pyridoxal phosphate enzymes: Mechanistic, structural, and evolutionary considerations. *Annu. Rev. Biochem.* **73**, 383–415 (2004).
2. A. Mozzarelli, S. Bettati, Exploring the pyridoxal 5′-phosphate-dependent enzymes. *Chem. Rec.* **6**, 275–287 (2006).
3. A. Sarup, O. M. Larsson, A. Schousboe, GABA transporters and GABA-transaminase as drug targets. *Curr. Drug Targets CNS Neurol. Disord.* **2**, 269–277 (2003).
4. K. A. Abrahams *et al.*, Inhibiting mycobacterial tryptophan synthase by targeting the inter-subunit interface. *Sci. Rep.* **7**, 9430 (2017).
5. D. Niks *et al.*, Allostery and substrate channeling in the tryptophan synthase bienzyme complex: Evidence for two subunit conformations and four quaternary states. *Biochemistry* **52**, 6396–6411 (2013).
6. K. Michalska *et al.*, Allosteric inhibitors of Mycobacterium tuberculosis tryptophan synthase. *Protein Sci.* **29**, 779–788 (2020).
7. J. F. Rocha, A. F. Pina, S. F. Sousa, N. M. F. S. A. Cerqueira, PLP-dependent enzymes as important biocatalysts for the pharmaceutical, chemical and food industries: A structural and mechanistic perspective. *Catal. Sci. Technol.* **9**, 4864–4876 (2019).
8. D. K. Romney, J. Murciano-Calles, J. E. Wehrmüller, F. H. Arnold, Unlocking reactivity of TrpB: A general biocatalytic platform for synthesis of tryptophan analogues. *J. Am. Chem. Soc.* **139**, 10769–10776 (2017).
9. M. Dick, N. S. Sarai, M. W. Martynowycz, T. Gonen, F. H. Arnold, Tailoring tryptophan synthase TrpB for selective quaternary carbon bond formation. *J. Am. Chem. Soc.* **141**, 19817–19822 (2019).
10. B. G. Caulkins *et al.*, Catalytic roles of βLys87 in tryptophan synthase: (15)N solid state NMR studies. *Biochim. Biophys. Acta* **1854**, 1194–1199 (2015).
11. B. G. Caulkins *et al.*, NMR crystallography of a carbanionic intermediate in tryptophan synthase: Chemical structure, tautomerization, and reaction specificity. *J. Am. Chem. Soc.* **138**, 15214–15226 (2016).
12. E. H. Cordes, W. P. Jencks, Semicarbazone formation from pyridoxal, pyridoxal phosphate, and their Schiff bases. *Biochemistry* **1**, 773–778 (1962).
13. B. G. Caulkins *et al.*, Protonation states of the tryptophan synthase internal aldimine active site from solid-state NMR spectroscopy: Direct observation of the protonated Schiff base linkage to pyridoxal-5′-phosphate. *J. Am. Chem. Soc.* **136**, 12824–12827 (2014).
14. J. Kraus, S. Sarkar, C. M. Quinn, T. Polenova, "Solid-state NMR spectroscopy of microcrystalline proteins" in *Annual Reports on NMR Spectroscopy*, G. A. Webb, Ed. (Academic Press, 2021), **vol. 102**, pp. 81–151.
15. A. K. Schütz, Solid-state NMR approaches to investigate large enzymes in complex with substrates and inhibitors. *Biochem. Soc. Trans.* **49**, 131–144 (2021).
16. M. Kovermann, P. Rogne, M. Wolf-Watz, Protein dynamics and function from solution state NMR spectroscopy. *Q. Rev. Biophys.* **49**, e6 (2016).
17. D. P. Frueh, Practical aspects of NMR signal assignment in larger and challenging proteins. *Prog. Nucl. Magn. Reson. Spectrosc.* **78**, 47–75 (2014).
18. G. R. Marshall *et al.*, Determination of a precise interatomic distance in a helical peptide by REDOR NMR. *J. Am. Chem. Soc.* **112**, 963–966 (2002).
19. M. L. Gilchrist Jr. *et al.*, Measurement of interfluorine distances in solids. *J. Magn. Reson.* **152**, 1–6 (2001).
20. J. E. Ollerenshaw, V. Tugarinov, L. E. Kay, Methyl TROSY: Explanation and experimental verification. *Magn. Reson. Chem.* **41**, 843–852 (2003).
21. W. P. Aue, E. Bartholdi, R. R. Ernst, Two-dimensional spectroscopy. Application to nuclear magnetic resonance. *J. Chem. Phys.* **64**, 2229 (1976).
22. S. Żerko, W. Koźmiński, Six- and seven-dimensional experiments by combination of sparse random sampling and projection spectroscopy dedicated for backbone resonance assignment of intrinsically disordered proteins. *J. Biomol. NMR* **63**, 283–290 (2015).
23. T. Wiegand *et al.*, Monitoring ssDNA binding to the DnaB helicase from Helicobacter pylori by solid-state NMR spectroscopy. *Angew. Chem. Int. Ed. Engl.* **55**, 14164–14168 (2016).
24. H. Fraga *et al.*, Solid-state NMR H-N-(C)-H and H-N-C-C 3D/4D correlation experiments for resonance assignment of large proteins. *ChemPhysChem* **18**, 2697–2703 (2017).
25. D. F. Gauto *et al.*, Aromatic ring dynamics, thermal activation, and transient conformations of a 468 kDa enzyme by specific ^1H-^{13}C labeling and fast magic-angle spinning NMR. *J. Am. Chem. Soc.* **141**, 11183–11195 (2019).
26. H. Singh *et al.*, Fast-microsecond dynamics of the protein-water network in the active site of human carbonic anhydrase II by solid-state NMR spectroscopy. *J. Am. Chem. Soc.* **141**, 19276–19288 (2019).
27. P. I. Aguion, J. Kirkpatrick, T. Carlomagno, A. Marchanka, Identification of RNA base pairs and complete assignment of nucleobase resonances by proton-detected solid-state NMR spectroscopy at 100 kHz MAS. *Angew. Chem. Int. Ed. Engl.* **60**, 23903–23910 (2021).
28. M. Lu *et al.*, Atomic-resolution structure of HIV-1 capsid tubes by magic-angle spinning NMR. *Nat. Struct. Mol. Biol.* **27**, 863–869 (2020).
29. M. T. Colvin *et al.*, Atomic resolution structure of monomorphic Aβ42 amyloid fibrils. *J. Am. Chem. Soc.* **138**, 9663–9674 (2016).
30. M. D. Tuttle *et al.*, Solid-state NMR structure of a pathogenic fibril of full-length human α-synuclein. *Nat. Struct. Mol. Biol.* **23**, 409–415 (2016).
31. V. S. Mandala *et al.*, Structure and drug binding of the SARS-CoV-2 envelope protein transmembrane domain in lipid bilayers. *Nat. Struct. Mol. Biol.* **27**, 1202–1208 (2020).
32. A. E. McDermott, F. J. Creuzet, A. C. Kolbert, R. G. Griffin, High-resolution magic-angle-spinning NMR spectra of protons in deuterated solids. *J. Magn. Reson.* **98**, 408–413 (1992).
33. E. K. Paulson *et al.*, Sensitive high resolution inverse detection NMR spectroscopy of proteins in the solid state. *J. Am. Chem. Soc.* **125**, 15831–15836 (2003).
34. V. Chevelkov, K. Rehbein, A. Diehl, B. Reif, Ultrahigh resolution in proton solid-state NMR spectroscopy at high levels of deuteration. *Angew. Chem. Int. Ed. Engl.* **45**, 3878–3881 (2006).
35. S. Asami, B. Reif, Proton-detected solid-state NMR spectroscopy at aliphatic sites: Application to crystalline systems. *Acc. Chem. Res.* **46**, 2089–2097 (2013).
36. R. Linser, V. Chevelkov, A. Diehl, B. Reif, Sensitivity enhancement using paramagnetic relaxation in MAS solid-state NMR of perdeuterated proteins. *J. Magn. Reson.* **189**, 209–216 (2007).
37. N. P. Wickramasinghe *et al.*, Nanomole-scale protein solid-state NMR by breaking intrinsic 1HT1 boundaries. *Nat. Methods* **6**, 215–218 (2009).
38. C. Öster, S. Kosol, J. R. Lewandowski, Quantifying microsecond exchange in large protein complexes with accelerated relaxation dispersion experiments in the solid state. *Sci. Rep.* **9**, 11082 (2019).
39. S. Penzel *et al.*, Protein resonance assignment at MAS frequencies approaching 100 kHz: A quantitative comparison of J-coupling and dipolar-coupling-based transfer methods. *J. Biomol. NMR* **63**, 165–186 (2015).
40. J. Stanek *et al.*, NMR spectroscopic assignment of backbone and side-chain protons in fully protonated proteins: Microcrystals, sedimented assemblies, and amyloid fibrils. *Angew. Chem. Int. Ed. Engl.* **55**, 15504–15509 (2016).
41. S. K. Vasa, H. Singh, K. Grohe, R. Linser, Assessment of a large enzyme-drug complex by proton-detected solid-state NMR without deuteration. *Angew. Chem. Int. Ed. Engl.* **58**, 5758–5762 (2019).
42. R. Linser, Side-chain to backbone correlations from solid-state NMR of perdeuterated proteins through combined excitation and long-range magnetization transfers. *J. Biomol. NMR* **51**, 221–226 (2011).
43. R. Linser, B. Bardiaux, V. Higman, U. Fink, B. Reif, Structure calculation from unambiguous long-range amide and methyl 1H-1H distance restraints for a microcrystalline protein with MAS solid-state NMR spectroscopy. *J. Am. Chem. Soc.* **133**, 5905–5912 (2011).
44. A. Bertarello *et al.*, Picometer resolution structure of the coordination sphere in the metal-binding site in a metalloprotein by NMR. *J. Am. Chem. Soc.* **142**, 16757–16765 (2020).
45. H. W. Orton *et al.*, Protein NMR resonance assignment without spectral analysis: 5D SOlid-state automated projection spectroscopY (SO-APSY). *Angew. Chem. Int. Ed. Engl.* **59**, 2380–2384 (2020).

46. J. Stanek *et al.*, Automated backbone NMR resonance assignment of large proteins using redundant linking from a single simultaneous acquisition. *J. Am. Chem. Soc.* **142**, 5793–5799 (2020).
47. M. Zinke *et al.*, Architecture of the flexible tail tube of bacteriophage SPP1. *Nat. Commun.* **11**, 5759 (2020).
48. T. Schubeis, J. Stanek, G. Pintacuda, Backbone assignment of crystalline E. coli maltose binding protein. *Biomol. NMR Assign.* **15**, 317–322 (2021).
49. W. T. Franks, K. D. Kloepper, B. J. Wylie, C. M. Rienstra, Four-dimensional heteronuclear correlation experiments for chemical shift assignment of solid proteins. *J. Biomol. NMR* **39**, 107–131 (2007).
50. S. Xiang, V. Chevelkov, S. Becker, A. Lange, Towards automatic protein backbone assignment using proton-detected 4D solid-state NMR data. *J. Biomol. NMR* **60**, 85–90 (2014).
51. S. Xiang, J. Biernat, E. Mandelkow, S. Becker, R. Linser, Backbone assignment for minimal protein amounts of low structural homogeneity in the absence of deuteration. *Chem. Commun. (Camb.)* **52**, 4002–4005 (2016).
52. M. Zinke *et al.*, Bacteriophage tail-tube assembly studied by proton-detected 4D solid-state NMR. *Angew. Chem. Int. Ed. Engl.* **56**, 9497–9501 (2017).
53. S. K. Vasa, H. Singh, P. Rovó, R. Linser, Dynamics and interactions of a 29 kDa human enzyme studied by solid-state NMR. *J. Phys. Chem. Lett.* **9**, 1307–1311 (2018).
54. M. Huber, A. Böckmann, S. Hiller, B. H. Meier, 4D solid-state NMR for protein structure determination. *Phys. Chem. Chem. Phys.* **14**, 5239–5246 (2012).
55. R. Linser *et al.*, Solid-state NMR structure determination from diagonal-compensated, sparsely nonuniform-sampled 4D proton-proton restraints. *J. Am. Chem. Soc.* **136**, 11002–11010 (2014).
56. C. Shi *et al.*, Atomic-resolution structure of cytoskeletal bactofilin by solid-state NMR. *Sci. Adv.* **1**, e1501087 (2015).
57. L. J. Mueller, M. F. Dunn, NMR crystallography of enzyme active sites: Probing chemically detailed, three-dimensional structure in tryptophan synthase. *Acc. Chem. Res.* **46**, 2008–2017 (2013).
58. J. D. Hartman, T. J. Neubauer, B. G. Caulkins, L. J. Mueller, G. J. O. Beran, Converging nuclear magnetic shielding calculations with respect to basis and system size in protein systems. *J. Biomol. NMR* **62**, 327–340 (2015).
59. J. B. Holmes *et al.*, Imaging active site chemistry and protonation states in tryptophan synthase: NMR-assisted crystallography of the α-aminoacrylate intermediate. *Proc. Natl. Acad. Sci. U.S.A.*, 10.1073/pnas.2109235119 (2022).
60. R. Linser, U. Fink, B. Reif, Narrow carbonyl resonances in proton-diluted proteins facilitate NMR assignments in the solid-state. *J. Biomol. NMR* **47**, 1–6 (2010).
61. A. Klein, S. K. Vasa, R. Linser, Automated projection spectroscopy in solid-state NMR. *J. Biomol. NMR* **72**, 163–170 (2018).
62. R. Linser, U. Fink, B. Reif, Proton-detected scalar coupling based assignment strategies in MAS solid-state NMR spectroscopy applied to perdeuterated proteins. *J. Magn. Reson.* **193**, 89–93 (2008).
63. R. Linser *et al.*, Proton-detected solid-state NMR spectroscopy of fibrillar and membrane proteins. *Angew. Chem. Int. Ed. Engl.* **50**, 4508–4512 (2011).
64. E. Barbet-Massin *et al.*, Rapid proton-detected NMR assignment for proteins with fast magic angle spinning. *J. Am. Chem. Soc.* **136**, 12489–12497 (2014).
65. D. H. Zhou *et al.*, Proton-detected solid-state NMR spectroscopy of fully protonated proteins at 40 kHz magic-angle spinning. *J. Am. Chem. Soc.* **129**, 11791–11801 (2007).
66. L. B. Andreas *et al.*, Protein residue linking in a single spectrum for magic-angle spinning NMR assignment. *J. Biomol. NMR* **62**, 253–261 (2015).
67. S. Xiang *et al.*, Sequential backbone assignment based on dipolar amide-to-amide correlation experiments. *J. Biomol. NMR* **62**, 303–311 (2015).
68. K. Kazimierczuk, A. Zawadzka, W. Koźmiński, Narrow peaks and high dimensionalities: Exploiting the advantages of random sampling. *J. Magn. Reson.* **197**, 219–228 (2009).
69. M. G. Jain *et al.*, Selective ^{1}H-^{1}H distance restraints in fully protonated proteins by very fast magic-angle spinning solid-state NMR. *J. Phys. Chem. Lett.* **8**, 2399–2405 (2017).
70. J. S. Retel *et al.*, Structure of outer membrane protein G in lipid bilayers. *Nat. Commun.* **8**, 2073 (2017).
71. T. Schubeis *et al.*, A β-barrel for oil transport through lipid membranes: Dynamic NMR structures of AlkL. *Proc. Natl. Acad. Sci. U.S.A.* **117**, 21014–21021 (2020).
72. N. Kulminskaya *et al.*, Access to side-chain carbon information in deuterated solids under fast MAS through non-rotor-synchronized mixing. *Chem. Commun. (Camb.)* **52**, 268–271 (2016).
73. N. Kulminskaya, S. K. Vasa, K. Giller, S. Becker, R. Linser, Asynchronous through-bond homonuclear isotropic mixing: Application to carbon-carbon transfer in perdeuterated proteins under MAS. *J. Biomol. NMR* **63**, 245–253 (2015).
74. E. Schmidt, P. Güntert, A new algorithm for reliable and general NMR resonance assignment. *J. Am. Chem. Soc.* **134**, 12817–12829 (2012).
75. A. Klein *et al.*, Solid-state NMR assignments of tryptophan synthase of S. typhimurium. Biological Magnetic Resonance Data Bank. https://bmrb.io/data_library/summary/index.php?bmrbId=51166. Deposited 4 November 2021.
76. D. L. Bryce, NMR crystallography: Structure and properties of materials from solid-state nuclear magnetic resonance observables. *IUCrJ* **4**, 350–359 (2017).
77. J. C. Facelli, D. M. Grant, Determination of molecular symmetry in crystalline naphthalene using solid-state NMR. *Nature* **365**, 325–327 (1993).
78. P. Hodgkinson, NMR crystallography of molecular organics. *Prog. Nucl. Magn. Reson. Spectrosc.* **118–119**, 10–53 (2020).
79. H. Zhang *et al.*, HIV-1 capsid function is regulated by dynamics: Quantitative atomic-resolution insights by integrating magic-angle-spinning NMR, QM/MM, and MD. *J. Am. Chem. Soc.* **138**, 14066–14075 (2016).
80. J. A. Gascón, E. M. Sproviero, V. S. Batista, QM/MM study of the NMR spectroscopy of the retinyl chromophore in visual rhodopsin. *J. Chem. Theory Comput.* **1**, 674–685 (2005).
81. C. Bonhomme *et al.*, First-principles calculation of NMR parameters using the gauge including projector augmented wave method: A chemist's point of view. *Chem. Rev.* **112**, 5733–5779 (2012).
82. J. D. Hartman, R. A. Kudla, G. M. Day, L. J. Mueller, G. J. O. Beran, Benchmark fragment-based (1)H, (13)C, (15)N and (17)O chemical shift predictions in molecular crystals. *Phys. Chem. Chem. Phys.* **18**, 21686–21709 (2016).
83. E. A. Engel *et al.*, A Bayesian approach to NMR crystal structure determination. *Phys. Chem. Chem. Phys.* **21**, 23385–23400 (2019).
84. S. Sharif, G. S. Denisov, M. D. Toney, H.-H. Limbach, NMR studies of solvent-assisted proton transfer in a biologically relevant Schiff base: Toward a distinction of geometric and equilibrium H-bond isotope effects. *J. Am. Chem. Soc.* **128**, 3375–3387 (2006).
85. M. Chan-Huot *et al.*, NMR studies of protonation and hydrogen bond states of internal aldimines of pyridoxal 5′-phosphate acid-base in alanine racemase, aspartate aminotransferase, and poly-L-lysine. *J. Am. Chem. Soc.* **135**, 18160–18175 (2013).
86. U. Sternberg *et al.*, ^{1}H line width dependence on MAS speed in solid state NMR - Comparison of experiment and simulation. *J. Magn. Reson.* **291**, 32–39 (2018).
87. Y. M. Huang *et al.*, Protonation states and catalysis: Molecular dynamics studies of intermediates in tryptophan synthase. *Protein Sci.* **25**, 166–183 (2016).
88. A. Hassan *et al.*, Sensitivity boosts by the CPMAS CryoProbe for challenging biological assemblies. *J. Magn. Reson.* **311**, 106680 (2020).
89. K. Kosiński, J. Stanek, M. J. Górka, S. Żerko, W. Koźmiński, Reconstruction of non-uniformly sampled five-dimensional NMR spectra by signal separation algorithm. *J. Biomol. NMR* **68**, 129–138 (2017).
90. Y. Shen, A. Bax, Protein backbone and sidechain torsion angles predicted from NMR chemical shifts using artificial neural networks. *J. Biomol. NMR* **56**, 227–241 (2013).